







A comparative analysis of the active galactic nucleus and star formation characteristics of broad- and narrow-line Seyfert 1 galaxies

K. S. Kurian^{1,2} , C. S. Stalin¹ , S. Rakshit³ , G. Mountrichas⁴ , D. Wylezalek⁵ , R. Sagar¹ , and M. Kissler-Patig⁶ 

¹ Indian Institute of Astrophysics, Block II, Koramangala, Bangalore, India e-mail: kshama.sara@gmail.com

² Pondicherry University, Puducherry, 605014, India

³ Aryabhata Research Institute of Observational Sciences, Manora Peak, Nainital 263002, India

⁴ Instituto de Física de Cantabria (CSIC-Universidad de Cantabria), Avenida de los Castros, 39005 Santander, Spain

⁵ Astronomisches Rechen-Institut, Zentrum für Astronomie der Universität Heidelberg, Monchhofstr. 12-14, 69120 Heidelberg, Germany

⁶ European Space Agency (ESA), European Space Astronomy Centre (ESAC), Camino Bajo del Castillo s/n, 28692 Villanueva de la 8 Canada, Madrid, Spain

ABSTRACT

We report here our comparative analysis of the active galactic nucleus (AGN) and star formation (SF) characteristics of a sample of narrow-line Seyfert 1 (NLS1) and broad-line Seyfert 1 (BLS1) galaxies. Our sample consisted of 373 BLS1 and 240 NLS1 galaxies and spanned the redshift $0.02 < z < 0.8$. The broad-band spectral energy distribution, constructed using data from the ultra-violet to the far-infrared, was modelled using CIGALE to derive the basic properties of our sample. We searched for differences in stellar mass (M_*), star formation rate (SFR), and AGN luminosity (L_{AGN}) in the two populations. We also estimated new radiation-pressure-corrected black hole masses for our sample of BLS1 and NLS1 galaxies. While the virial black hole mass (M_{BH}) of BLS1 galaxies is similar to their radiation-pressure-corrected M_{BH} values, the virial M_{BH} values of NLS1 galaxies are underestimated. We found that NLS1 galaxies have a lower M_{BH} of $\log(M_{BH} [M_\odot]) = 7.45 \pm 0.27$ and a higher Eddington ratio of $\log(\lambda_{Edd}) = -0.72 \pm 0.22$ than BLS1 galaxies, which have $\log(M_{BH} [M_\odot])$ and λ_{Edd} values of 8.04 ± 0.26 and -1.08 ± 0.24 , respectively. The distributions of M_* , SFR, and specific star formation (sSFR = SFR/ M_*) for the two populations are indistinguishable. This analysis is based on an independent approach and contradicts reports in the literature that NLS1 galaxies have a higher SF than BLS1 galaxies. While we found that L_{AGN} increases with M_* , L_{SF} flattens at high M_* for both BLS1 and NLS1 galaxies. The reason may be that SF is suppressed by AGN feedback at M_* higher than $\sim 10^{11} M_\odot$ or that the AGN fuelling mechanism is decoupled from SF. Separating the sample into radio-detected and radio-undetected subsamples, we found no difference in their SF properties suggesting that the effect of AGN jets on SF is negligible.

Key words. galaxies: active - galaxies: Seyfert - galaxies: star formation - galaxies: jets

1. Introduction

Narrow-line Seyfert 1 (NLS1) galaxies are a peculiar category of active galactic nuclei (AGN). Since they were identified as a separate class of objects by Osterbrock & Pogge (1985), they have attracted the attention of the AGN community because their properties are peculiar. They have relatively narrow permitted optical emission lines with a full width at half maximum of the $H\beta$ emission line $< 2000 \text{ km s}^{-1}$, a flux ratio of the [OIII] to $H\beta$ line < 3 , strong Fe II lines, steep soft X-ray spectra (Boller et al. 1996), and rapid X-ray variability (Rani et al. 2017). The observed properties of NLS1 galaxies are thought to be caused by low-mass black holes at their centres, with masses ranging from $\sim 10^6$ to $10^8 M_\odot$, which accrete at a very high rate (Grupe & Mathur 2004; Williams et al. 2018). However, from spectropolarimetric observations of the radio-loud NLS1 galaxy PKS 2004–447, Baldi et al. (2016) found a polarized $H\alpha$ line, with a width much larger than the width seen in total light, thereby yielding a higher black hole mass (M_{BH}) similar to that known for typical radio-loud AGN. Moreover, Calderone et al. (2013)

and Viswanath et al. (2019) reported based on fitting the accretion disk spectra to the observed spectra of NLS1 galaxies that their M_{BH} values are similar to their broad-line counterparts, namely broad-line Seyfert 1 (BLS1) galaxies. They are found to show optical flux variations within a night (Klimek et al. 2004; Paliya et al. 2013; Kshama et al. 2017; Ojha et al. 2019; Turner et al. 2022). On a year-like timescale, they are also found to vary in the optical (Rakshit & Stalin 2017) and infrared bands (Rakshit et al. 2019).

The hosts of NLS1 galaxies, from observations available as of today, are known to be spirals, often barred and with pseudo-bulges (Mathur et al. 2012; Zhou et al. 2007; Antón et al. 2008; León Tavares et al. 2014; Kotilainen et al. 2016; Järvelä et al. 2018; Olguín-Iglesias et al. 2020; Varglund et al. 2022). A small fraction (about 5%) of the NLS1 galaxies is known to emit in the radio band, and only a handful of the sources that emit in the radio band are found to have large-scale relativistic jets (Doi et al. 2012; Rakshit et al. 2018; Doi et al. 2019; Vietri et al. 2022a). A small fraction of radio-loud NLS1 galaxies are also known to be emitters of γ -rays, as observed by the *Fermi* Gamma-ray

Space Telescope (Abdo et al. 2009; Paliya et al. 2019). However, radio-loud objects are thought to be hosted by elliptical galaxies. Given the uncertainties on the morphology of the hosts of NLS1 galaxies, it becomes imperative to understand the hosts of these systems in relation to BLS1 galaxies.

It has been suggested by Mathur (2000) that NLS1 galaxies are gas-rich and young sources with ongoing star formation (SF). This also explains the high accretion and high metallicity (Nagao et al. 2002) in some NLS1 galaxies. From low-resolution mid-infrared spectroscopy of a very small number of NLS1 and BLS1 galaxies, Sani et al. (2010) found that NLS1 galaxies have higher SF activities than BLS1 galaxies of the same luminosity. The signatures of outflow in their spectra are also stronger than in BLS1 galaxies (Jha et al. 2022). Given the evidence of outflows and considering that NLS1 are galaxies with a high Eddington ratio that may produce high radiative feedback, it is also interesting to determine whether the AGN and the SF characteristics of the host galaxies are connected.

The cosmic SF rate and black hole accretion rate follow a similar evolution over cosmic time. Both of them show a peak at around $z \sim 2$ that is followed by a sharp decline towards the present age (Madau & Dickinson 2014; Dickinson et al. 2003; Babić et al. 2007; Hopkins et al. 2007). Observational evidence also indicates a close correlation between (a) the mass of the central super-massive black hole and the galaxy luminosity (Kormendy & Richstone 1995; Marconi & Hunt 2003; Gültekin et al. 2009), (b) mass of the super-massive black hole and the galaxy bulge mass (Magorrian et al. 1998; McLure & Dunlop 2002), and (c) the mass of the super-massive black hole and the velocity dispersion (Ferrarese & Merritt 2000; Gebhardt et al. 2000; Merritt & Ferrarese 2001). All available observations thus indicate that black holes (their formation and growth) and their host galaxy properties are fundamentally coupled. Studies are also available in the literature about the connection between AGN and their host galaxies, but the results of these studies disagree. For example, there are reports that the AGN luminosity (L_{AGN}) correlates with the star formation rate (SFR) of their host galaxies (Lanzuisi et al. 2017; Zhuang & Ho 2020), while some studies have found either a weak or no correlation between SFR and L_{AGN} (Harrison et al. 2012; Shimizu et al. 2017; Stanley et al. 2017). The conflicting results from different studies might in part be due to the sample used for the studies and the analysis methods that were followed.

A close correlation is known to exist between SF and stellar mass (M_*) for SF galaxies of the main sequence (MS; Daddi et al. 2007; Elbaz et al. 2007). In the case of AGN, a few studies indicated that the host galaxies of AGN lie on or above the MS (Silverman et al. 2009; Santini et al. 2012; Zhuang & Ho 2022), while other studies reported evidence that AGN host galaxies lie below the MS. (Bongiorno et al. 2012; Mullaney et al. 2015; Shimizu et al. 2015). One of the reasons for these results that are known today might be that the AGN activity plays an important role in regulating the SF in their host galaxies via the feedback processes that operate in them. Thus, the effect of the AGN on their host galaxies is still a matter of debate, and a systematic investigation of the AGN activity and its impact on the SF activity in their hosts is indeed needed to assess the nature of the connection between AGN and SF activity.

We aim to investigate the nature of the host galaxies of NLS1 galaxies and determine how they compare with the host galaxy properties of a comparison sample of BLS1 galaxies. This investigation will also enable us to understand the effect of the central AGN in NLS1 and BLS1 galaxies has on their hosts in the context of them (as is generally thought) being powered by

low- and high-mass black holes, respectively. The main controversies surrounding NLS1 galaxies and their association with BLS1 galaxies are (1) the differences in the black hole mass, with NLS1 galaxies thought to have a lower black hole mass than BLS1 galaxies, (2) the high Eddington ratios of NLS1 with respect to BLS1 galaxies, and (3) the claim that NLS1 have higher SFRs and are hosted by young gas-rich galaxies with respect to BLS1 galaxies. Although many comparative studies of NLS1 and BLS1 are published, their samples have included very few objects, or they only compared one of the galaxy properties. In this work, we therefore carried out a comparative analysis of the physical parameters of the AGN and the host galaxies in populations of NLS1 and BLS1 galaxies. The paper is organised as follows. In Section 2 we describe the selection of the sample and the data collection. The broad-band spectral energy distribution (SED) fitting is described in Section 3. In section 4 we investigate the similarities and/or differences of the host galaxy properties of NLS1 and BLS1 galaxies, and in the final section, we summarise our results.

2. Sample and data

Our initial sample of NLS1 galaxies was taken from Rakshit et al. (2017), while the BLS1 galaxies were taken from those obtained in the process of arriving at the NLS1 galaxy sample by Rakshit et al. (2017). They span the redshift $0.02 < z < 0.8$. The sample consisted of 11101 and 14886 NLS1 and BLS1 galaxies. According to Hatziminaoglou et al. (2009), the far-infrared (FIR) emission in AGN host galaxies mostly arises from SF. To characterise the SF properties of galaxies hosting AGN, the inclusion of FIR data is therefore indeed important because it can constrain the AGN contribution to the infrared luminosity of the host galaxy, and it improves the SFR estimation without AGN contamination (Stanley et al. 2018). When FIR photometry is not included, the SFR is known to be systematically underestimated (Masoura et al. 2018). Therefore, we selected all sources that were detected by the *Herschel* Space Observatory in at least one band of 100, 160, 250, 350, and 500 μm . With the FIR constraint, our sample for this study consisted of 240 NLS1 galaxies and 373 BLS1 galaxies. Based on the available multi-wavelength data set, this is the best sample that can be constructed for a comparative analysis of the SF characteristics of BLS1 and NLS1 galaxies. This supersedes the single earlier study (Sani et al. 2010) with a manifold increase in the number of sources, and we use a different approach. The FIR selection criteria bias the sample towards high SFR galaxies. However, this bias affects both BLS1 and NLS1 galaxies similarly, and hence, it does not affect the results of a comparative analysis of the two types of galaxies. The observed fluxes and their corresponding errors for our sample of BLS1 galaxies and NLS1 galaxies are given in the Appendix in Tables ?? and ??, respectively. We note that the selected sample of 240 NLS1 and 373 BLS1 galaxies was for a broad-band SED modelling, but the final sample selected for the comparative study was based on an SED fitting (see Section 3).

We collected the broad-band photometric data for all our sample sources based on observations carried out by various ground- and space-based telescopes. In the ultra-violet (UV) region, we used data in the near-UV (NUV) and far-UV (FUV) bands from the Galaxy Evolution Explorer (GALEX; Morrissey et al. 2007) archives. In the optical band, we used data in ugriz photometric bands from the Sloan Digital Sky Survey (SDSS¹). Near infra-red (NIR) data in J, H, and K bands were taken from

¹ <https://www.sdss4.org/dr17/>

the Two Micron All-Sky Survey (2MASS; Skrutskie et al. 2006). For the mid-IR, we used data in the W1, W2, W3, and W4 bands from the *Wide-field Infrared Survey Explorer* (WISE; Wright et al. 2010), and for the FIR, we used data from the Herschel Space Observatory (*Herschel*; Pilbratt et al. 2010). The photometric data and their associated errors used in this work thus come from different instruments with various point spread functions and methods adopted to derive the magnitudes. Both BLS1 and NLS1 galaxies are also known to show flux variations, and therefore, the non-simultaneous measurements collected across different wavelengths affect the SED modelling. However, as both the BLS1 and NLS1 used in this work suffer from the same issues of (a) the non-uniformity of the aperture sizes used for the magnitude determinations and (b) the non-simultaneity of flux measurements, their impact, if any, on a comparative analysis of the derived physical quantities may not be significant.

3. Spectral energy distribution modelling using CIGALE

We derived various parameters of the host galaxies of our sample using the Code Investigating GALaxy Emission (CIGALE; Boquien et al. (2019)). CIGALE is a spectral energy distribution (SED) modelling code that relies on the availability of photometric data in multiple wavelengths to derive the properties of galaxies by comparing the modelled SEDs to observed SEDs. CIGALE works on the principle of energy balance (i.e. the energy emitted in the mid- and far-IR bands by dust matches the energy absorbed by dust in the visible and UV bands) and uses a Bayesian analysis method to derive the model parameters (Boquien et al. 2019). The fitting routine adopted here takes into account (a) the radiation emitted by stars that dominate the optical region from 3000 to 4000 Å, (b) the radiation from dust heated by stellar emission that dominates the FIR region, and (c) the radiation from the accretion disk in AGN, which peaks in the UV region, as well as the scattered radiation by the dusty torus, which peaks in the mid-IR region. We briefly describe the modules we adopted for the SED fitting below.

1. *sfhdelayed module*: To model the SEDs, we used the delayed star formation history (SFH), which is expressed as

$$SFR(\tau) \propto \frac{t}{\tau^2} * \exp\left(-\frac{t}{\tau}\right) \quad \text{for } 0 < t < t_o. \quad (1)$$

Here, τ is the time at which the SFR peaks, and t_o is the age of the onset of SF. In this model, the SFR decreases smoothly after peaking at $t = \tau$. Using simulated realistic SEDs of galaxies with AGN and adopting various SFH models in the CIGALE modelling of the simulated SEDs, Ciesla et al. (2015) have shown that the *sfhdelayed* model provides reliable M^* and SFR measurements and should be preferred over the single exponentially decreasing and double exponentially decreasing models. Moreover, Mountrichas et al. (2022) recently compared the *sfhdelayed* with the newest *sfhdelayedbq* available in CIGALE, which allows both an instantaneous recent variation of the SFR upwards (burst) and downwards (quenching; Ciesla et al. 2017; Boquien et al. 2019). The authors found that the two SFH models provide a consistent SFR. We therefore adopted the *sfhdelayed model* in this work.

2. *BC03 module*: To generate the spectrum for the adopted SFH, we adopted the single stellar population library of Bruzual & Charlot (2003) for a Chabrier (2003) initial mass

function (IMF) and solar metallicity. We adopted a value of 10 Myr as the age separating the old from the young stellar populations.

3. *dustatt_modified_CF00 module*: The dust present in galaxies absorbs UV to optical radiation and re-emits them in the mid- and far-IR bands. To model the attenuation of starlight by the dust in galaxies, we used the *dustatt_modified_CF00* module, which implements the model of Charlot & Fall (2000). This model assumes two power-law attenuation curves of the form $A(\lambda) \propto \lambda^\alpha$, one for the birth cloud (BC), and the other for the interstellar medium (ISM). For the attenuation due to the ISM and BC, we assumed a power-law index α of -0.7 .
4. *Dale et al. (2014) module*: To model the IR emission from the dust heated by radiation from stars, we used the templates from Dale et al. (2014). This also comprises the radiation from dust heated by the AGN. As the AGN model is included separately, we set the AGN contribution in Dale et al. (2014) model to 0. This model is parametrised as

$$dM_{dust}(U) \propto U^{-\alpha} dU. \quad (2)$$

Here, U is the radiation field intensity, and M_{dust} is the mass of the dust heated by the radiation field. We chose α to have a range of values as given in Table 1.

5. *AGN module*: Along with the SF, the AGN in the hosts contribute to the observed emission from galaxies, and it is difficult to distinguish this because the AGN and stars both emit in the UV band, and a large fraction of this UV emission is absorbed by dust in galaxies and is re-emitted at mid- and far-IR wavelengths. To model the contribution of AGN to the observed emission from galaxies, we used the SKIRTOR (Stalevski et al. 2016) model to parametrise the AGN component to the SED. This is based on SKIRT, a 3D radiative transfer code that includes obscuration by the torus (Baes et al. 2011).

The complete set of parameters we used to build the SEDs of our sample of galaxies is given in Table 1. The parameters we adopted for the SED modelling are similar to those used by Mountrichas et al. (2021a); Vietri et al. (2022b); Koutoulidis et al. (2022) and were modified to suit our sample of sources. The physical parameters from this SED analysis were derived through the analysis of the likelihood distribution. Examples of SED fits to the data are given in Fig. 1. We note that an SED analysis of this type can have errors due to (a) the different aperture sizes used in the photometric measurements taken from different instruments, and (b) the photometric measurements being not simultaneous. Our sample sources are known to vary, which may lead to errors in the model fitting. The median χ^2 per degrees of freedom for the BLS1 sample is 2.5. Therefore, for all subsequent analyses, we used only the sources for which the SED fitting returned a χ^2 per degrees of freedom values ranging from 0.5 (a conservative limit) to 5 (twice the median value of BLS1). With these criteria, we were left with a final sample of 319 BLS1 and 205 NLS1 galaxies. All further analyses were restricted to this reduced sample. These two samples match in redshift, as shown in Fig. 2. The mean z -values of this reduced sample are 0.33 and 0.35 for BLS1 and NLS1 galaxies, respectively. A KS test p -value of 0.14 shows that the redshift distribution of both types of galaxies is similar. From previous studies using CIGALE, it is known that the uncertainties in CIGALE are underestimated, and the true uncertainties in SFR and stellar mass are at least 0.3 dex (Jarvis et al. (2019) and the references therein). Some of the physical parameters obtained from CIGALE modelling of the observed SEDs are given in Table 2 and Table 3 for the BLS1 and NLS1 galaxies, respectively.

Table 1: Parameters adopted for the SED fitting using CIGALE

Parameter	Description	Value
SFH - Delayed Model		
Age_main	Stellar age	200, 500, 700, 1000, 2000 3000, 4000, 5000 Myr
τ_{main}	e-folding time of the stellar population	1500, 2000, 3000, 4000, 5000, 7000, 10000, 12000 Myr
Age_burst, τ_{burst}	Age and e-folding time of the late burst	10000 Myr, 50 Myr
F_burst	Mass fraction of the late burst population	0.0, 0.005, 0.01, 0.015, 0.02, 0.05, 0.10, 0.15, 0.18, 0.20
Stellar Emission Bruzual & Charlot (2003)		
IMF	Initial mass function	Chabrier
Z	abundance	0.02
Dust attenuation Charlot & Fall (2000)		
Av_ISM	V band extinction in the ISM	0.2, 0.3, 0.4, 0.5, 0.6, 0.7, 0.8, 0.9, 1.0, 1.5, 2.0, 2.5, 3.0, 3.5, 4.0
Nebular Emission		
log U	logarithm of the Ionization parameter	-2.0
Line_width	Width of the line in km/s	300.0
Dust Dale et al. (2014)		
α	power law index of the sum of the dust templates	2.0
frac_AGN	AGN fraction	0.0
AGN module <i>skirtor2016</i> : Stalevski et al. (2016)		
i	viewing angle	30, 70
Delta	power law index of the optical slope	-0.36
f_AGN	AGN fraction	0.0, 0.1, 0.2, 0.3, 0.4, 0.5, 0.6, 0.7, 0.8, 0.9, 0.99
E(B-V)	Extinction in the polar direction	0.0, 0.2, 0.4

Table 2: Parameters derived for the sample of BLS1 galaxies by fitting the SED with CIGALE. The table in full is available in the electronic version of the article.

index	SDSS ID	RA	Dec	z	FWHM	L ₅₁₀₀	L _{AGN}	log ₁₀ (SFR)	L _{SF}	M _*	log ₁₀ (sSFR)	M _{BH} (virial)	M _{BH} (RP)	log ₁₀ (λ_{Edd})
		deg	deg		km s ⁻¹	erg s ⁻¹	erg s ⁻¹	M _⊙ yr ⁻¹	erg s ⁻¹	M _⊙	Gyr ⁻¹	M _⊙	M _⊙	
1	1768-53442-0193	187.7193	14.5515	0.1151	3649.26	43.49	43.68	0.68	44.22	10.37	-0.69	7.54	7.42	-1.85
2	7235-56603-0309	37.2306	-5.1918	0.3656	2451.56	44.06	44.82	1.6	45.14	11.06	-0.47	7.5	7.84	-1.13
3	0470-51929-0431	135.589	0.5725	0.3262	3568.51	44.24	45.08	1.73	45.27	10.91	-0.18	7.92	8.06	-1.09
4	1616-53169-0453	189.39	13.3185	0.1511	2464.65	43.67	44.37	0.94	44.48	10.35	-0.42	7.3	7.48	-1.23
5	0471-51924-0172	136.9312	1.5578	0.1642	4905.72	43.71	44.28	-0.51	43.04	11.28	-2.78	7.92	7.7	-1.53

4. Results

In this section, we compare the AGN and SF properties of BLS1 and NLS1 galaxies and show that the AGN activity might affect the SF in the host galaxy.

4.1. Host galaxy properties: Star formation rate, stellar mass, and specific star formation rate

We show in Fig. 3 the distribution of the SFR and M_{*} for our sample of BLS1 and NLS1 galaxies. For the NLS1 galaxies, we found a mean log(SFR M_⊙yr⁻¹) = 1.18 ± 0.33, while for the BLS1 galaxies, we found a mean log(SFR M_⊙yr⁻¹) = 1.18 ± 0.41. We thus found no difference in the SFR between NLS1

and BLS1 galaxies. A KS test indicates that the distributions are similar at the 90% level, with a *p*-value of 0.07. The distribution of M_{*} for our sample of NLS1 and BLS1 galaxies is shown in the right panel of Fig. 3. We found a mean M_{*} of log(M_{*}[M_⊙]) = 10.74 ± 0.25 and 10.78 ± 0.24 for the NLS1 and BLS1 galaxies, respectively. From a KS test, we found that the distribution of M_{*} is similar for the BLS1 and NLS1 galaxies, with a *p*-value of 0.71.

We show in Fig. 4 the evolution of the SFR and sSFR (SFR/M_{*}) with *z*. The SFR and sSFR are binned in redshift, and the geometric mean of the SFR and sSFR in each redshift bin is plotted over the individual data points. We also computed the SFR of main sequence (MS) galaxies (SFR_{MS}) using the relation

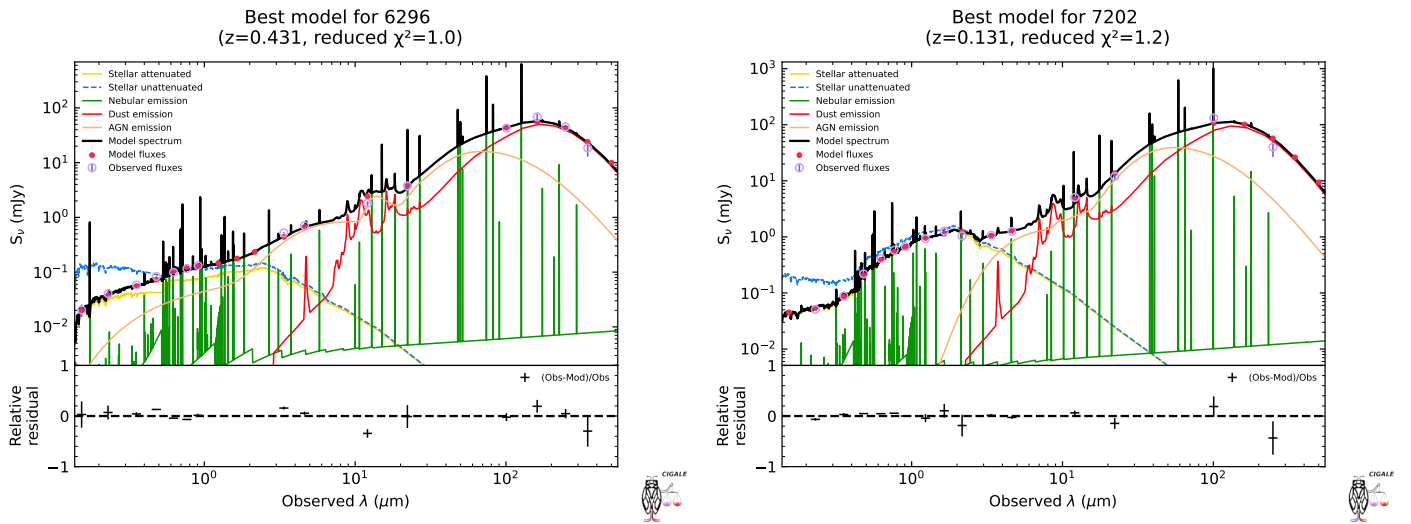


Fig. 1: Examples of the observed SED along with the best-fit SED from CIGALE for one NLS1 galaxy (left panel) and one BLS1 galaxy (right panel). The open and filled symbols correspond to the observed and modelled flux densities. The goodness of the fit, represented by the reduced χ^2 , is given at the top of each plot. The residuals of the fit are given at the bottom of each panel.

Table 3: Parameters derived for the sample of NLS1 galaxies by fitting the SED with CIGALE. The table in full is available in the electronic version of the article.

index	SDSS ID	RA	Dec	z	FWHM	L_{5100}	L_{AGN}	$\log_{10}(\text{SFR})$	L_{SF}	M_*	$\log_{10}(\text{sSFR})$	M_{BH} (virial)	M_{BH} (RP)	$\log_{10}(\lambda_{Edd})$
		deg	deg		km s ⁻¹	erg s ⁻¹	erg s ⁻¹	M_{\odot} yr ⁻¹	erg s ⁻¹	M_{\odot}	Gyr ⁻¹	M_{\odot}	M_{\odot}	
1	7386-56769-0752	156.753	48.5549	0.5985	1512	43.46	44.74	0.56	44.1	10.44	-0.88	6.76	7.23	-0.6
2	2751-54243-0611	226.5035	14.2612	0.1432	1950	44.21	45.25	1.62	45.16	10.38	0.25	7.38	7.96	-0.82
3	1959-53440-0473	157.1984	31.7738	0.2067	1364	43.76	45.02	1.3	44.84	10.71	-0.4	6.83	7.51	-0.6
4	2216-53795-0107	171.5435	26.6513	0.2949	2039	43.5	45.36	1.64	45.18	10.29	0.35	7.04	7.3	-0.05
5	6445-56366-0710	163.0503	32.2317	0.7843	1194	43.62	44.38	1.14	44.68	10.44	-0.3	6.64	7.36	-1.1

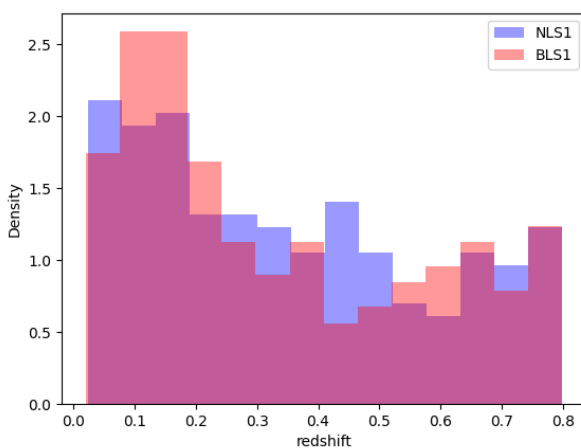


Fig. 2: Redshift distribution for the best SED fits of the NLS1 and BLS1 galaxies

described in Schreiber et al. (2015),

$$\log(\text{SFR}_{MS}) = m - m_0 + a_0 * r - a_1 [\max(0, m - m_1 - a_2 r)]^2. \quad (3)$$

Here, $m_0 = 0.5 \pm 0.07$, $a_0 = 1.5 \pm 0.15$, $a_1 = 0.3 \pm 0.008$, $m_1 = 0.36 \pm 0.3$, $a_2 = 2.5 \pm 0.6$, $r = \log_{10}(1+z)$, and $m =$

$\log_{10}(M_*/M_{\odot})$. The generalised relation arrived at by Schreiber et al. (2015) was (a) based on objects that span a range of redshifts from $0.3 < z < 5.0$, and (b) the SFR was estimated by combining direct UV and reprocessed UV light in the FIR. The redshifts of our sample sources overlap with the range investigated by Schreiber et al. (2015) and also use both UV to FIR photometric points to obtain the SFR. **The Schreiber et al. (2015) MS relation extends down to $z = 0$ (see Ciesla et al. 2017).** We therefore adopted the relation of Schreiber et al. (2015). Analytical expressions from the literature for the MS may introduce systematic effects. These effects are due to the different methods that were applied to calculate the host galaxy properties, for instance, to the different models and parametric grid for the SED fitting, to the different photometric coverage, the different selection criteria, and even to the different definitions of the MS (Mountrichas et al. 2021b). Mountrichas et al. (2021b) compared in their Fig. 6 the SFR calculations of CIGALE (using sfhdelayed) with the SFR from Schreiber et al. (2015) and Whitaker et al. (2014). They found that at low redshifts ($z < 1.5$), the SFR from CIGALE tends to be lower than the SFR from Schreiber et al. (2015). However, this difference is about 0.25 dex and does not affect the results and conclusions of this paper (e.g. the right panel in 4). The shaded yellow region in Fig. 4 represents the sSFR of MS galaxies as described in Equation 3 for the stellar mass range of BLS1 and NLS1 galaxies. The mean $\log(\text{sSFR})$ of NLS1 and BLS1 galaxies tends to lie on the SF main sequence in the sSFR- z plane. This indicates that the SF

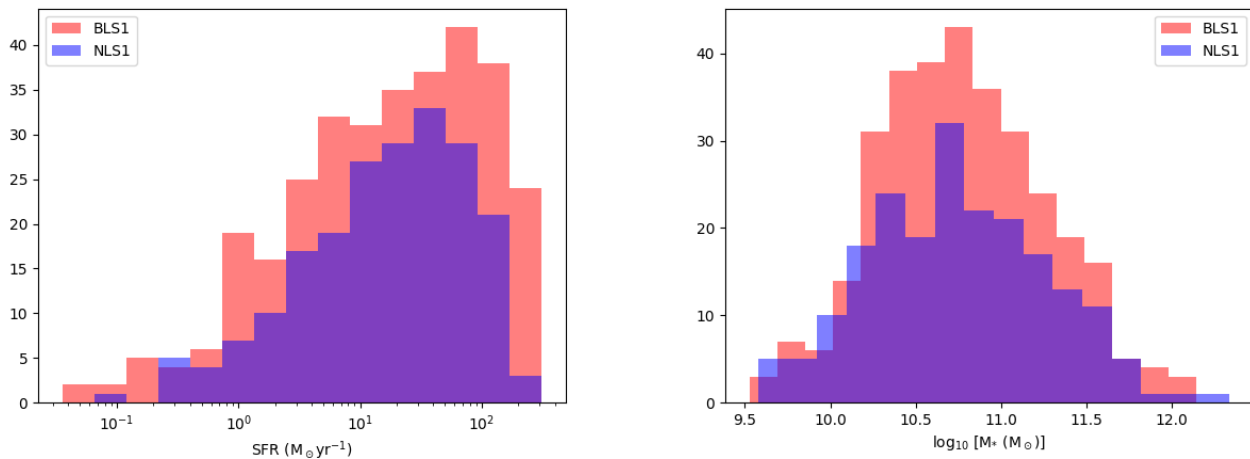


Fig. 3: Histogram of the SFR (left) and M_* (right) for our sample of BLS1 and NLS1 galaxies.

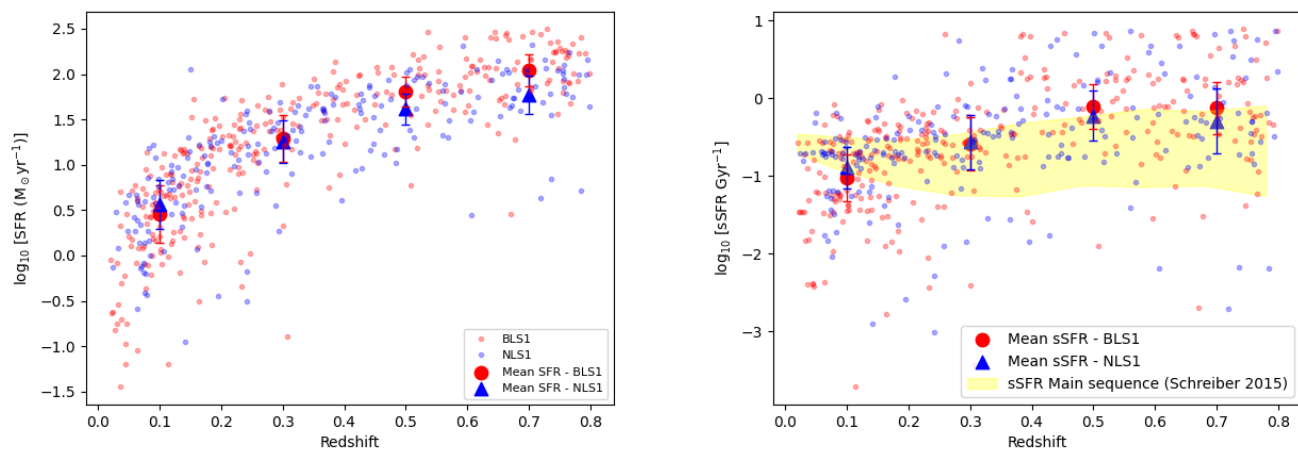


Fig. 4: Star formation properties of Seyfert 1 galaxies. Left panel: Redshift-binned mean values of SFR of BLS1 (red) and NLS1 (blue) galaxies. Right panel: Redshift-binned sSFR of BLS1 (red) and NLS1 (blue) galaxies. The shaded yellow region represents the sSFR of MS galaxies for the stellar mass range of the BLS1 and NLS1 galaxies.

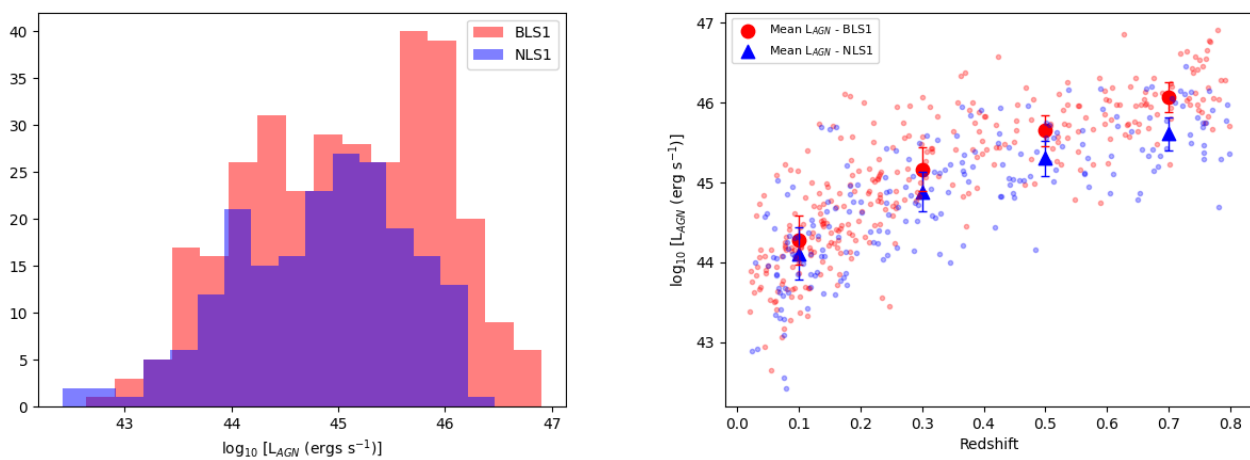


Fig. 5: AGN luminosity of Seyfert 1 galaxies. Left panel: Distribution of L_{AGN} for BLS1 and NLS1 galaxies. Right panel: Variation in L_{AGN} with redshift.

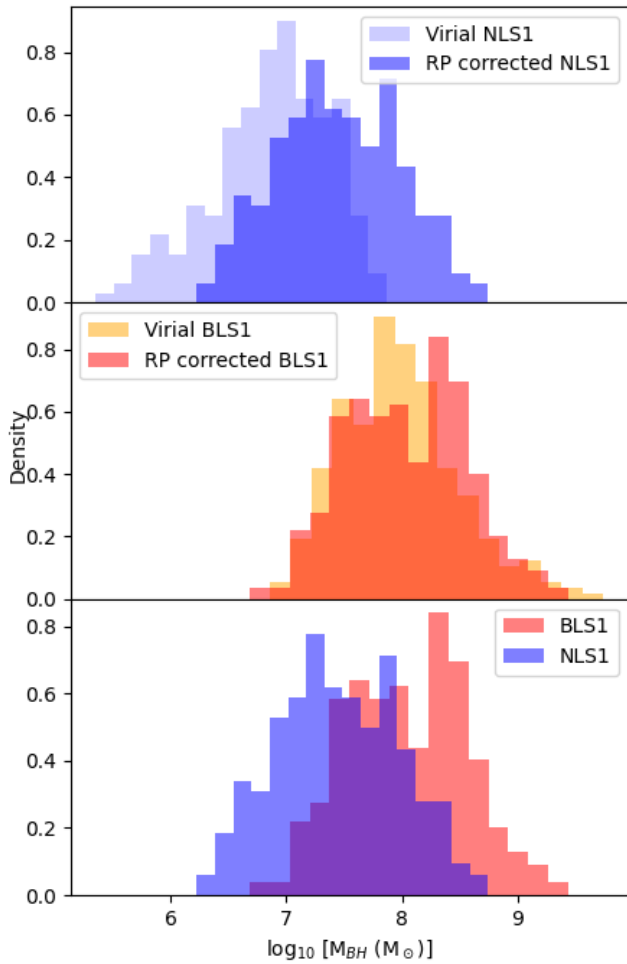


Fig. 6: Distribution of M_{BH} values of BLS1 and NLS1 galaxies. *Top panel:* Virial (light blue) and radiation-pressure-corrected (dark blue) M_{BH} values of NLS1 galaxies. *Middle panel:* Virial (orange) and radiation-pressure-corrected (red) M_{BH} values of BLS1 galaxies. *Bottom:* Radiation-pressure-corrected M_{BH} values of NLS1 (blue) and BLS1 (red) galaxies.

properties of Seyfert 1 galaxies are similar to the SF properties of MS galaxies, and this agrees with studies that showed AGN to be preferentially hosted in star-forming galaxies (Mullaney et al. 2012).

4.2. Active galactic nucleus properties: Active galactic nucleus luminosity, black hole mass, and Eddington ratio

To model the AGN emission, we used the *skirtor2016* module in CIGALE (see Table 1). SKIRTOR is a clumpy two-phase torus model (Stalevski et al. 2016) and is based on SKIRT (Baes et al. 2011), which is a 3D radiative transfer code². In this module, the parameter f_{AGN} defines the relative strength between AGN and galaxy components, and we varied f_{AGN} from 0.0 to 0.99. L_{AGN}

is one of the output parameters of the *skirtor2016* module and is the sum of the AGN disk luminosity and AGN dust luminosity. We show in the left panel in Fig. 5 the distribution L_{AGN} for our sample of BLS1 and NLS1 galaxies. We found mean $\log(L_{AGN})$ values of 45.06 ± 0.44 and 44.84 ± 0.39 for BLS1 and NLS1 galaxies, respectively. This shows that BLS1 galaxies tend to have L_{AGN} slightly higher than NLS1 galaxies. The KS test also confirms that the distribution of L_{AGN} for BLS1 and NLS1 galaxies is different, with a p -value of 0.001. When binned in z , the NLS1 galaxies have low L_{AGN} than the BLS1 galaxies (see Fig. 5 right panel).

To estimate the Eddington ratio, we need robust estimates of black hole masses. It is generally thought that NLS1 galaxies are powered by low-mass black holes (Grupe & Mathur 2004; Williams et al. 2018) compared to BLS1 galaxies (but see also Calderone et al. (2013); Baldi et al. (2016); Viswanath et al. (2019) for an alternative view). According to Marconi et al. (2008), while determining M_{BH} from the use of virial theorem to the broad emission lines in AGN spectra, the effect of radiation pressure needs to be taken into account. When the radiation pressure is not included, the M_{BH} values in sources radiating close to the Eddington limit would be underestimated. Marconi et al. (2008) arrived at an empirical relation to determine M_{BH} that also considers the effect of radiation pressure. We therefore recalculated the M_{BH} values for the sources in our sample of BLS1 and NLS1 galaxies using the relation given in Marconi et al. (2008),

$$\frac{M_{BH}}{M_{\odot}} = \tilde{f} \left(\frac{V_{H\beta}}{1000 \text{ km s}^{-1}} \right)^2 \left(\frac{L_{5100}}{10^{44} \text{ ergs s}^{-1}} \right)^{0.5} + \tilde{g} \left(\frac{L_{5100}}{10^{44} \text{ ergs s}^{-1}} \right). \quad (4)$$

Here, $V_{H\beta}$ is the full width at half maximum of the $H\beta$ emission line, L_{5100} represents the luminosity at 5100 \AA , and \tilde{f} and \tilde{g} are the scale factors that take the physical and geometrical properties of the broad-line region into account. The parameter g depends on the cloud mass via the assumed column density and sets the relative importance of gravity and radiation pressure. We used a $\log(\tilde{f})$ value of 6.13 and $\log(\tilde{g})$ value of 7.72, following Marconi et al. (2008).

For the virial M_{BH} , we used the values given in Rakshit et al. (2017), which were estimated as follows:

$$M_B = f R_{BLR} \Delta v^2 / G. \quad (5)$$

Here, Δv is the full width at half maximum of the broad emission line, and R_{BLR} is the radius of the broad-line region, determined as

$$\log \left(\frac{R_{BLR}}{lt - day} \right) = K + \alpha \times \log \left(\frac{\lambda L_{\lambda}(5100 \text{ \AA})}{10^{44} \text{ ergs s}^{-1}} \right), \quad (6)$$

where the values of K and α are 1.527 and 0.533, respectively, taken from Bentz et al. (2013). Considering a spherical distribution of clouds, the scale factor $f = 3/4$ (Rakshit et al. 2017). We show in Fig. 6 the distribution of the virial and pressure-corrected M_{BH} values for both BLS1 and NLS1 galaxies in the top two panels. For the BLS1 galaxies, the distribution of the virial and pressure-corrected M_{BH} values is nearly similar, with a mean $\log(M_{BH}[M_{\odot}])$ of 7.98 ± 0.25 and 8.04 ± 0.26 , respectively. However, the KS test rejects the null hypothesis that the distributions are indeed drawn from the same population with a p -value of 0.001. For the NLS1 galaxies, the distributions of

² <https://skirt.ugent.be/root/index.html>

the virial M_{BH} values slightly overlap the distribution of the pressure-corrected M_{BH} values, but both distributions are indeed different based on the KS test statistics ($p = 8.7 \times 10^{-16}$). In the bottom panel of Fig. 6, we show the distribution of the pressure-corrected M_{BH} values for both NLS1 (mean $\log(M_{BH}[M_{\odot}]) = 7.45 \pm 0.27$) and BLS1 galaxies (mean $\log(M_{BH}[M_{\odot}]) = 8.03 \pm 0.26$). Although the two distributions overlap, the NLS1 galaxies have M_{BH} values that are lower than those of the BLS1 galaxies. From the KS test statistics ($p = 7.9 \times 10^{-18}$), we found that the pressure-corrected M_{BH} distribution of the BLS1 and NLS1 galaxies is indeed different.

When we only consider the virial M_{BH} values in NLS1 and BLS1 galaxies, the NLS1 galaxies in our sample have a mean M_{BH} value of $\log(M_{BH}[M_{\odot}]) = 6.86 \pm 0.25$, while the BLS1 galaxies have a mean value of $\log(M_{BH}[M_{\odot}]) = 7.98 \pm 0.25$. NLS1 galaxies are found to be powered by AGN with black hole masses that are almost an order of magnitude lower than BLS1 galaxies. In contrast, after taking into account the effect of radiation pressure from ionising photons, the difference in the M_{BH} values between BLS1 and NLS1 galaxies was reduced. However, NLS1 galaxies still have lower M_{BH} values than BLS1 galaxies. For NLS1 galaxies, we found a pressure-corrected mean $\log(M_{BH}[M_{\odot}])$ of $7.45 \pm 0.27 M_{\odot}$, while for BLS1 galaxies, we found a radiation-pressure-corrected mean $\log(M_{BH}[M_{\odot}]) = 8.04 \pm 0.26 M_{\odot}$. This means that the increase in BH mass of NLS1 after correction for radiation pressure is about 0.65 dex, or a factor of 5. This agrees with the results of Marconi et al. (2008), who found that when radiation pressure is taken into account, the BH masses of NLS1 are higher by a factor of 5.

Using the radiation-pressure-corrected mean M_{BH} values, we estimated the Eddington ratio $\lambda_{Edd} = L_{AGN} / L_{Edd}$, where $L_{Edd} = 1.3 \times 10^{38} \times M_{BH} / M_{\odot} (\text{ergs}^{-1})$. We found that NLS1 galaxies have a higher Eddington ratio of $\log_{10}(\lambda_{Edd}) = -0.72 \pm 0.22$ than BLS1 galaxies, which have a mean $\log_{10}(\lambda_{Edd}) = -1.08 \pm 0.24$. The NLS1 galaxies have a higher Eddington ratio than BLS1 galaxies, which is supported by a KS test statistics with a p -value of 2.48×10^{-10} . When binned in redshift, at each z bin, NLS1 galaxies have lower M_{BH} values than BLS1 galaxies (top panel of Fig. 7). In each z bin, NLS1 galaxies also have higher λ_{Edd} than BLS1 galaxies (Fig. 7 bottom panel).

4.3. Correlation between star formation rate and active galactic nucleus luminosity

Previous studies of the correlation between SFR and L_{AGN} are inconclusive. A weak or absent correlation was reported (Stanley et al. 2015, 2017), but also a strong correlation (Lanzuisi et al. 2017; Ichikawa et al. 2017; Zhuang & Ho 2020; Masoura et al. 2018, 2021). According to Stanley et al. (2015), the observed flat relation may be due to short-timescale luminosity variation (driven by the accretion rate) in AGN, which may have washed out any inherent relation between SFR and L_{AGN} . Recently, Kim et al. (2022) found that AGN with a higher Eddington ratio and stronger outflows are hosted by galaxies with a high SFR, which is suggestive of no AGN feedback in quenching SF. These contradicting results might be due to the different methods that were used to estimate SFR and L_{AGN} . We show in the left panel of Fig. 8 the correlation of SFR against L_{AGN} . Our results show a strong positive correlation between SFR and L_{AGN} , with a slope of 0.7 and 0.6 for BLS1 and NLS1 galaxies, respectively. This is close to the slope value of 0.8 determined by Netzer (2009).

This positive correlation could be an artefact due to the effects of M_{*} and z (Stanley et al. 2017). To overcome the effect of M_{*} , we compared the sSFR with AGN luminosities and

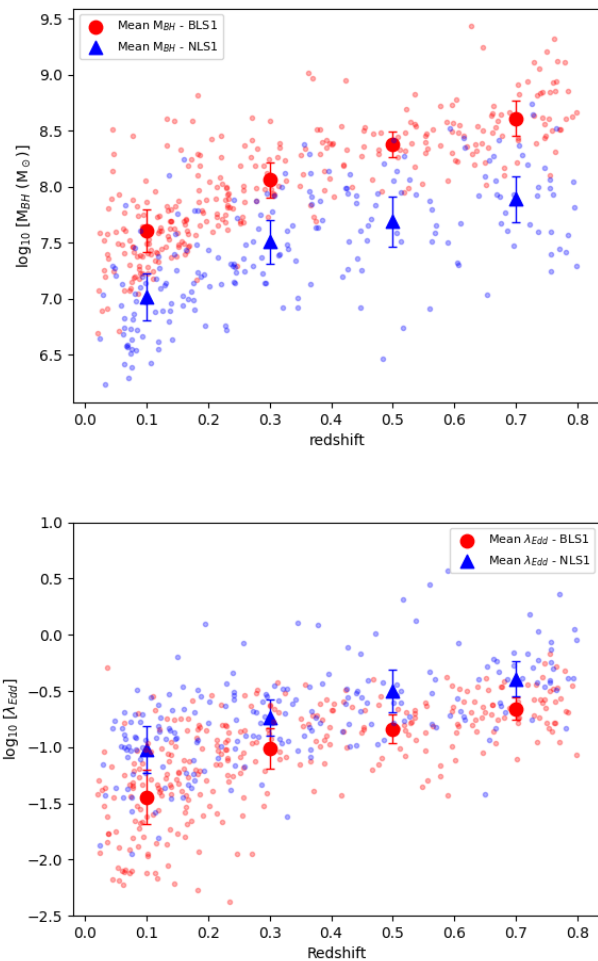


Fig. 7: Variation in the redshift-binned M_{BH} (top) and λ_{Edd} (bottom) for BLS1 (red) and NLS1 (blue) galaxies.

found a much weaker correlation between the two properties. The slightly high sSFRs at high AGN luminosities is a redshift effect, which can be seen by comparing Fig. 4 and Fig. 5. Thus, taking both M_{*} and z into consideration, we found no significant correlation between the sSFR and L_{AGN} . Our results seem to indicate no impact of AGN feedback on both populations of Seyfert galaxies, in agreement with Stanley et al. (2017), who found a flat relation of SFR with L_{AGN} for AGN with a range of luminosities. We note that the flat relation between SFR and AGN luminosity is attributed to the different timescales of the SF and AGN activity (Hickox et al. 2014). However, the spread in the sSFRs of AGN host galaxies is much larger than the 1σ scatter in MS galaxies, which is around 0.3 dex (Schreiber et al. 2015). This large scatter in the sSFRs of AGN host galaxies with respect to MS galaxies might be due to the impact of AGN on their host galaxies (Scholtz et al. 2018).

4.4. Active galactic nucleus versus starbursts: Which dominates?

We show in Fig. 9 the location of our sample of sources in the R versus $\log(L_{SF}/L_{AGN})$ plane. Here, R is defined as the ratio of SFR to the SFR_{MS} for the corresponding M_{*} and z , where SFR_{MS} is estimated using Eq. 3. L_{SF} is defined as the integrated

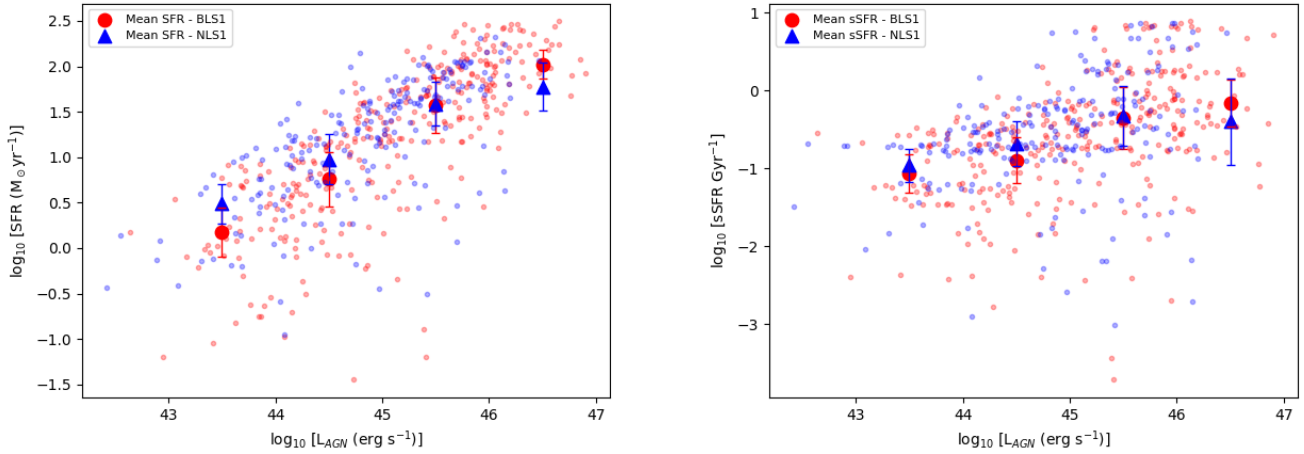


Fig. 8: Binned SFR (left) and sSFR (right) against L_{AGN} for NLS1 (blue) and BLS1 (red) galaxies.

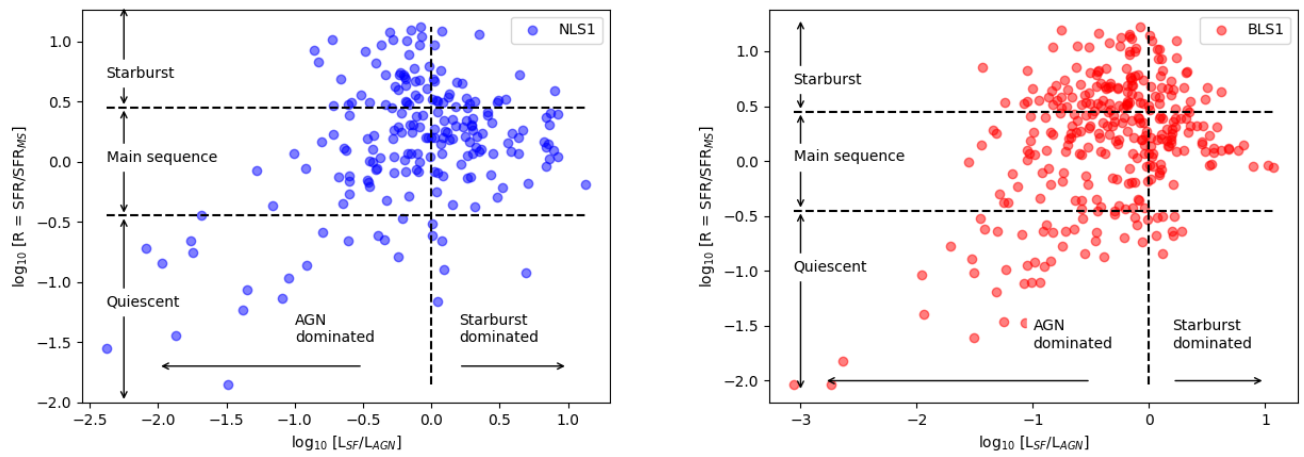


Fig. 9: Ratio of SFR to the main-sequence SFR of the corresponding stellar mass and redshift, $R = SFR/SFR_{MS}$, vs. the ratio of SF luminosity to AGN luminosity, L_{SF}/L_{AGN} .

luminosity due to the SF between 8 and 1000 μm in its host galaxy. It is calculated from the SFR using the relation of Kennicutt (1998) corrected for the Chabrier IMF (Hopkins et al. 2010),

$$\frac{L_{SF}}{L_{\odot}} = \frac{SFR}{1.1 \times 10^{-10}} \text{ erg s}^{-1}. \quad (7)$$

Shimizu et al. (2015) considered R to be the distance of a source from the SF MS. They considered objects with $\log(R) > 1\sigma$ to have enhanced SF. The 1σ scatter in MS galaxies is 0.3 dex (Schreiber et al. 2015). Conservatively, we considered a stricter limit of 1.5σ and defined $\log(R) > 0.45$ dex as galaxies with enhanced SF, $-0.45 < \log(R) < 0.45$ as MS galaxies, and $\log(R) < -0.45$ dex as galaxies with suppressed SF. In the sample of BLS1 galaxies, 35% are above the MS, 48% are on the MS, and 17% are below the MS, whereas of the NLS1 galaxies, 31% are above the MS, 57% are on the MS, and 12% are below the MS. The R -value estimated using the expressions in the literature may introduce systematic effects. However, in this paper, these systematics do not affect the overall results and conclusions because we compare the R between BLS1 and NLS1,

and thus, these systematics would affect both population measurements in the same way.

From Netzer (2009), we define a boundary in $\log(L_{SF}/L_{AGN})$ wherein sources with $\log(L_{SF}/L_{AGN}) > 0$ occupy the region dominated by starbursts and sources with $\log(L_{SF}/L_{AGN}) < 0$ occupy the region dominated by AGN.

We found that 71% of the BLS1 galaxies are AGN dominated, but only 55% of the NLS1 galaxies are AGN dominated. This also indicates that NLS1 are more strongly dominated by starbursts (45%) than BLS1 galaxies (29%). While this is true, we recall that the SFR and sSFR properties are similar for both NLS1 and BLS1, as described in Section 4.1. Thus, that NLS1 galaxies are more strongly dominated by starbursts than BLS1 galaxies is largely driven by the differences in the AGN luminosities and not by their SF properties.

4.5. Impact of active galactic nucleus activity on star formation

Observations are inconclusive about the role of AGN feedback in quenching SF and its connection to the host galaxy evolution.

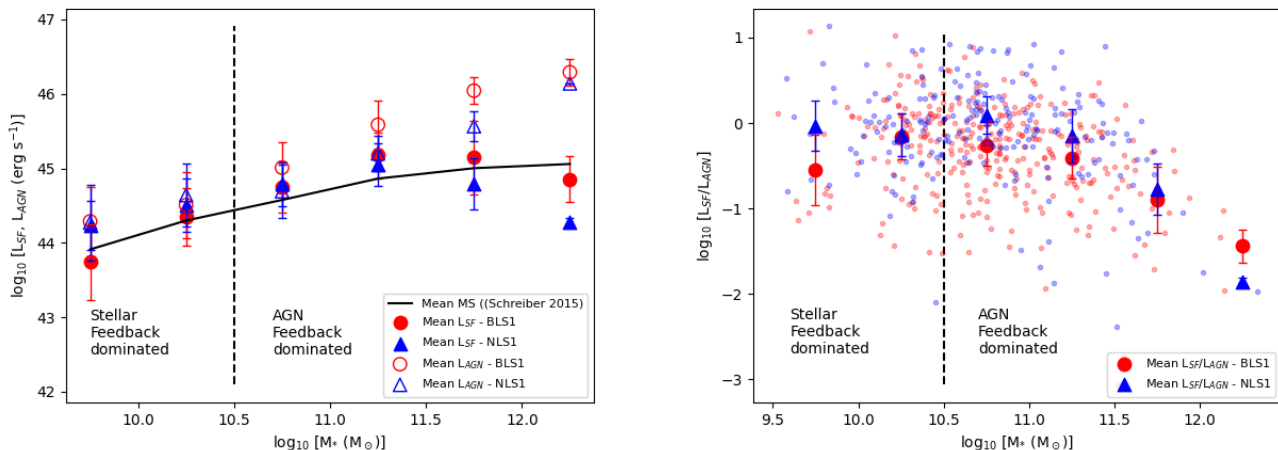


Fig. 10: Star formation luminosity (L_{SF}) and AGN luminosity (L_{AGN}) vs. stellar mass M_* (left). Ratio of L_{SF} to L_{AGN} vs. stellar mass. (right)

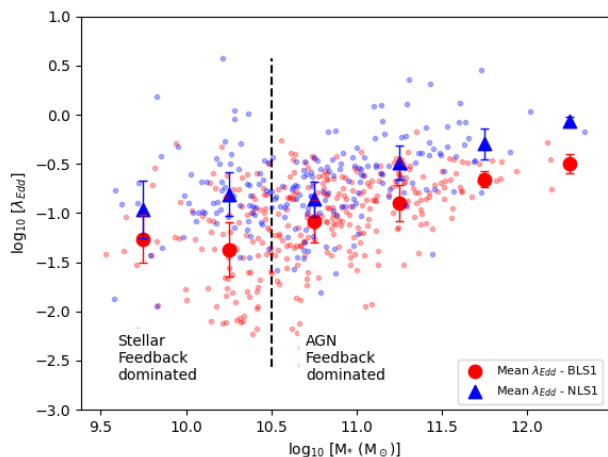


Fig. 11: Eddington ratio (λ_{Edd}) vs. stellar mass (M_*).

However, simulations of galaxy evolution are found to overpredict the high-mass end of the stellar mass function, and to account for this quenching of SF, the AGN feedback process is invoked (Bower et al. 2012). Observationally, the number density of galaxies per logarithmic mass bin is found to have a decreasing trend with mass, with a sharp cut-off at $\sim 10^{10.5} M_{\odot}$ (Baldry et al. 2012; Crain et al. 2015). Towards the low-mass end, supernova feedback is thought to play a role in regulating SF, while at the high-mass end, feedback from AGN is invoked to play a role (Crain et al. 2015). In high-redshift quasar hosts, a spatial anti-correlation is observed between the wind component of [OIII] and $H\alpha$ that traces the SF in the host galaxy (Cano-Díaz et al. 2012). This could be evidence of quasar winds quenching SF within their disks (Capelo et al. 2023).

To investigate the role of feedback, if any, in our sample of BLS1 and NLS1 galaxies, we compare their L_{SF} and L_{AGN} luminosities with stellar mass in the left panel of Fig. 10. We also mark the change in the feedback modes from stellar feedback to AGN feedback for the transition mass of $3 \times 10^{10} M_{\odot}$, as known in the literature (eg. Baldry et al. 2012) and through simulations

(e.g. Crain et al. 2015). For all further studies, we only considered the regime that is dominated by AGN feedback.

For both NLS1 and BLS1, the L_{SF} initially increases with stellar mass, but then flattens at high stellar masses, while L_{AGN} monotonically increases with M_* up to the high stellar mass bin. In the left panel of Fig. 10, we also plot the mean $\log(L_{SF})$ of MS galaxies (solid black line), using Equation 5 for comparison. The L_{SF} of NLS1 and BLS1 galaxies closely follow the relation of MS galaxies up to $M_* \sim 10^{11.5}$, beyond which it deviates. For further clarity, in the right panel of Fig. 10, we show the change in L_{SF}/L_{AGN} ratio with respect to stellar mass. Mullaney et al. (2012) found that for stellar masses lower than $10^{11} M_{\odot}$, the L_{SF}/L_{AGN} ratio remains constant, which they attributed to the availability of a common gas reservoir that regulates the AGN activity and SF. Our results agree with Mullaney et al. (2012) for the same range of stellar masses.

From FIRE-3³ cosmological simulations with haloes in the mass range of $10^{12} - 10^{13} M_{\odot}$, galaxies with AGN feedback are found to have quenched SF. Alternatively, galaxies without AGN are found to actively form stars regardless of their mass (Byrne et al. 2023). These simulations also agree with observations (Peng et al. 2010; Muzzin et al. 2013; Tomczak et al. 2014), which indicate a reduced SF in galaxies with a stellar mass higher than $10^{10.5} M_{\odot}$, which corresponds to a halo mass of $\sim 10^{12} M_{\odot}$.

We found that L_{SF}/L_{AGN} decreases with stellar mass. **One of the reasons for this decrease might be** negative AGN feedback at higher stellar masses (see the right panel of Fig. 10). This result is in line with simulations (e.g. Scholtz et al. 2018; Byrne et al. 2023). To verify the decreasing trend in L_{SF}/L_{AGN} , we estimated the Spearman correlation coefficient for objects with a stellar mass greater than $10^{10.5} M_{\odot}$. The correlation coefficient and p-value for the BLS1 L_{SF}/L_{AGN} and stellar mass are -0.30 and $3.8e-6$, respectively. The correlation coefficient and p-value for the NLS1, L_{SF}/L_{AGN} , and stellar mass is -0.43 and $1.1e-7$, respectively. These values suggest a weak negative correlation between L_{SF}/L_{AGN} and M_* for the high stellar mass range. Our results from the analysis of BLS1 and NLS1 galaxies therefore agree with simulations and with other observations in the litera-

³ Feedback In Realistic Environments (FIRE) project website: <http://fire.northwestern.edu>

ture. In Appendix B.1, we also show that the redshift effects on this correlation are negligible.

We also explore the change in Eddington ratio with stellar mass in Fig. 11. For the regime dominated by AGN feedback, the Eddington ratio increases with stellar mass, indicating an increasing radiative feedback with stellar mass, with more radiative feedback expected in NLS1 galaxies than BLS1 galaxies. Similar to the analysis done for L_{SF}/L_{AGN} , we verified the increasing trend by estimating the Spearman correlation coefficient for the Eddington ratio and M_* . The correlation coefficient and p-value for the BLS1 Eddington ratio and stellar mass are 0.40 and $6.1e-10$, respectively. The correlation coefficient and p-value for the NLS1 Eddington ratio and stellar mass are 0.58 and $4.5e-14$, respectively. These values suggest a weak positive correlation between the Eddington ratio and stellar mass for the high stellar mass range for BLS1 and a relatively strong positive correlation for NLS1. For AGN with high Eddington ratios, the radiative feedback from AGN can heat gas or remove gas from the host galaxies and suppress SF. This could be one reason for the decreasing trend in L_{SF}/L_{AGN} with increasing stellar mass at high stellar masses for NLS1 when compared to BLS1 galaxies.

Based on simulations, Bollati et al. (2023) have found that radiative feedback from AGN can limit the gas inflow that powers the SMBH and can also affect the host galaxy by suppressing the SF through gas removal by AGN winds in the nuclear (< 1 kpc) region. This imprint of AGN radiation is manifested at high accretion rates, wherein the gas in the central nuclear region is swept away, leading to a quenching of the SF. From spatially resolved observations of galaxies hosting AGN and normal galaxies, Lammers et al. (2023) found that in galaxies hosting AGN, SFR is suppressed in the central region (kpc scale) compared to normal galaxies. Although these observations recognise that AGN feedback has an effect close to the central regions of their host galaxies, the effect of AGN feedback affecting SF on the kiloparsec galaxy scale is uncertain (Fiore et al. 2017).

An alternative scenario that can explain the decreasing trend in L_{SF}/L_{AGN} or the flattening of L_{SF} for high stellar masses is the decoupling of AGN fuelling from SF. Mountrichas et al. (2021b, 2022) proposed that in low stellar mass ranges ($< 10^{11} M_{\odot}$), the cold gas could fuel both the AGN and SF, whereas for high stellar mass ranges, the AGN-fuelling mechanism may be decoupled from SF. This scenario would also explain the positive trend seen in AGN and SF with respect to stellar mass for $M_* < 10^{11} M_{\odot}$ in the left panel of Fig. 10.

The MS galaxies are also known to flatten at high M_* (Schreiber et al. 2015; Popesso et al. 2019). One of the reasons for this flattening in MS galaxies according to semi-analytical and hydrodynamical simulations might be the suppression of SF by SMBH feedback through outflows or jets that quench the bulge component and also prevent the cooling of gas in the disk component by feeding energy into the circumgalactic medium through jets and lobes (see Section 4.1 of Popesso et al. (2019)). Alternatively, the shape of the MS, including the flattening at high M_* , could be an outcome of the complex interplay between the morphology of the galaxies and their environment, and might not solely be due to stellar mass Popesso et al. (2019).

The BLS1 and NLS1 galaxies differ in their large-scale environment (Järvelä et al. 2017), and the galaxy environment may also be different among the individual sources analysed in this work. The environment can have a strong impact on the AGN activity as well as on SF, as shown in simulations (Singh et al. 2023; Rihtaršič et al. 2024). It is also likely that the nuclear regions of BLS1 and NLS1 galaxies host complex mergers that are not seen in ground-based optical/infrared images. This is sup-

ported by the identification of two galaxies in the act of merging in an NLS1 galaxy using high-resolution adaptive optical J-band imaging (Paliya et al. 2020). Spatially resolved observations of a large sample of sources are needed to fully understand the effect of AGN feedback and the spatial scales at which they are prevalent.

The host morphology of BLS1 galaxies is likely to be spiral galaxies (McLeod & Rieke 1995; Hunt & Malkan 1999; Orban de Xivry et al. 2011). Similarly, NLS1 galaxies are also frequently found in disk systems (Järvelä et al. 2018; Varglund et al. 2022, 2023). At low redshifts, Orban de Xivry et al. (2011) found a median bulge-to-total ratio (B/T) of 0.39 in BLS1s and 0.17 in NLS1s and further stated that NLS1 have pseudo-bulges while BLS1 have a mix of classic and pseudo-bulges. However, it is also known that the bulge-to-total ratio increases with stellar mass (e.g. Lang et al. 2014). The growth of bulges in massive galaxies corresponds to a decline in gas mass fractions and SFRs (e.g. Papovich et al. 2015). Star formation is linked to the disk component, which is the main driver of the MS relation. The growth of the bulge increases the stellar mass of a galaxy, but does not alter its SFR (Dimauro et al. 2022). It is therefore possible that due to the growth of the galaxy bulge at high stellar masses in Seyfert 1 galaxies, the contribution from the disk component towards SFR decreases, thus showing a flattened SFR. This may also decouple AGN fuelling from SF and would explain why the Eddington ratio increases with stellar mass while the SFR flattens or decreases.

4.6. Effect of jets on star formation

To investigate the effects of relativistic jets on the SF characteristics of our sample of BLS1 and NLS1 galaxies, we cross-correlated our sample with the sources in the Faint Images of the Radio Sky at Twenty centimeters (FIRST; Becker et al. 1995) survey. We found 70 radio-detected BLS1 (or 21% of the sample) and 29 radio-detected NLS1 (14%). We show in Fig. 12 the 1.4 GHz luminosity of the radio-detected sources against their SFR. We also show in the same figure the relation between the radio luminosity at 1.4 GHz and the SFR for star-forming galaxies (Magnelli et al. 2014). The FIRST-detected sources have a higher radio luminosity than expected for SF galaxies. This confirms the presence of relativistic jets in our radio-detected sample of BLS1 and NLS1 galaxies. We also show in Fig. 12 the variation in sSFR with z for our sample of radio-detected and radio undetected sources compared with the sSFR of normal SF galaxies. We found that the sSFR of radio-detected and radio undetected sources in our sample is similar to the sSFR of normal star-forming galaxies. We therefore conclude that the role of AGN jets, if any, in altering the SF characteristics in our sample is negligible. However, we note that available observational results in the literature indicate that radio jets affect the SF characteristics of their hosts (Duggal et al. 2024; Nandi et al. 2023).

5. Summary

We used the multi-band photometric data from the UV to the FIR to investigate the AGN and host galaxy properties of BLS1 and NLS1 galaxies. The findings of this work are summarised below.

1. The SFR and sSFR of NLS1 galaxies are similar to those of BLS1 galaxies. The logarithm of the mean SFR for BLS1 and NLS1 galaxies is 1.18 ± 0.41 and $1.18 \pm 0.33 M_{\odot}/\text{yr}$, respectively. Similarly, the logarithm of the mean stellar masses is 10.78 ± 0.24 and $10.74 \pm 0.25 M_{\odot}$ for BLS1 and

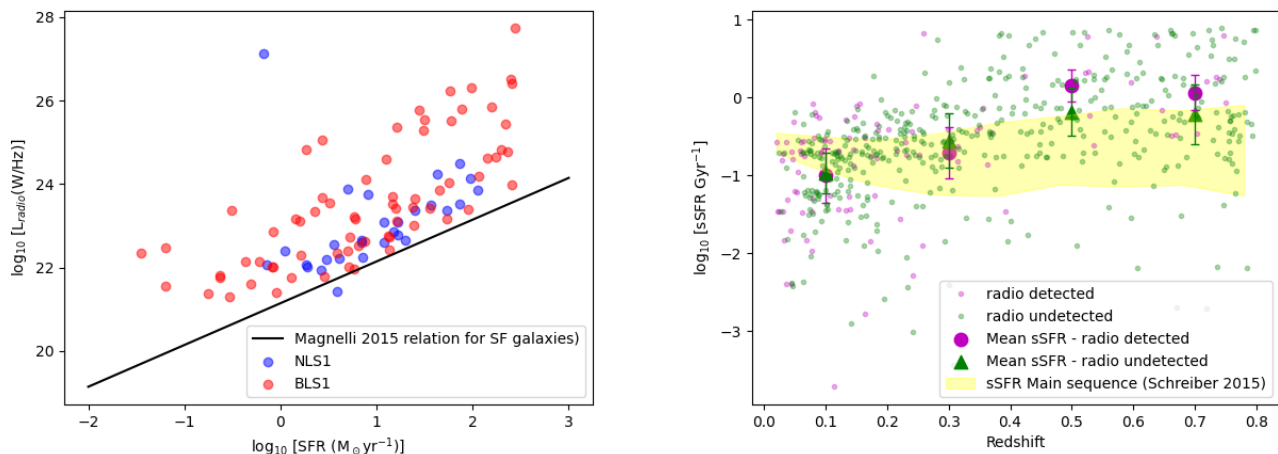


Fig. 12: Comparison of radio-detected and radio-undetected Seyfert 1 galaxies. Left panel: Radio luminosity at 1.4 GHz vs. the corresponding SFR. The black line shows the relation followed by star-forming galaxies. Right panel: Location of the radio-detected and radio-undetected Seyfert 1 galaxies in the sSFR- z plane.

NLS1 galaxies, respectively. Thus, there is no difference in the SF properties and stellar masses in our sample of broad- and narrow-line Seyfert 1 galaxies.

2. The logarithm of the mean sSFRs of NLS1 and BLS1 galaxies in each z bin tends to lie on the SF main sequence in the sSFR- z plane. This tends to indicate that the SF properties of Seyfert 1 galaxies are similar to the SF properties of MS galaxies.
3. The mean virial M_{BH} estimates are similar to the mean radiation-pressure-corrected M_{BH} values for BLS1 galaxies. However, for NLS1 galaxies, the virial M_{BH} are underestimated. This is might be because the high radiation pressure dilutes the effects of gravity in NLS1 galaxies (Marconi et al. 2008).
4. NLS1 galaxies have a lower mean $\log (M_{\text{BH}} [\text{M}_{\odot}])$ value of 7.45 ± 0.27 than BLS1 galaxies, which have a mean $\log (M_{\text{BH}} [\text{M}_{\odot}])$ of 8.04 ± 0.26 . This is true even when they are binned in redshift. This indicates that NLS1 are powered by lower-mass black holes than BLS1 galaxies.
5. BLS1 galaxies have more L_{AGN} than NLS1 galaxies. We found a mean $\log(L_{\text{AGN}})$ of $44.84 \pm 0.39 \text{ erg s}^{-1}$ and $45.07 \pm 0.44 \text{ erg s}^{-1}$ for NLS1 and BLS1 galaxies, respectively.
6. NLS1 have higher λ_{Edd} than BLS1 galaxies. The reason might be that NLS1 galaxies are hosted in gas-rich sources with efficient black hole fuelling mechanisms such as bars (Mathur 2000) and pseudo-bulges (Mathur et al. 2012), compared to BLS1 galaxies. For NLS1 galaxies, the mean logarithm of λ_{Edd} is -0.72 ± 0.22 , while for BLS1 galaxies, the mean logarithm of λ_{Edd} is -1.08 ± 0.24 .
7. We found a strong positive correlation between SFR and L_{AGN} for both BLS1 and NLS1 galaxies. When the effects of M_{\star} and z were taken into account, no correlation was found.
8. Using the $\log(L_{\text{SF}}/L_{\text{AGN}}) \geq 0$ as an indicator of starburst-dominated sources, we found that 45% of the NLS1 are starburst dominated compared to 29 % of the BLS1 galaxies. However, this is driven by the differences in the AGN luminosities of BLS1 and NLS1 galaxies.
9. When comparing the $\log(L_{\text{SF}})$ and $\log(L_{\text{AGN}})$ ratio with stellar mass, we find that as $\log(L_{\text{AGN}})$ increases with stellar mass, $\log(L_{\text{SF}})$ flattens at high stellar masses for both NLS1 and BLS1 galaxies. This may be due to AGN activity, which

might play a role in suppressing star formation at high stellar masses ($> 10^{11} \text{ M}_{\odot}$) or to AGN fuelling, which might be decoupled from SF. However, the role played by other factors such as environment and/or merging as well as the different timescales of AGN and SF activity cannot be ruled out.

10. When separated into radio-detected and radio-undetected sub-samples, we found no difference in the SF characteristics between these two sub-samples. The relativistic jets in these sub-samples have no impact on the SF properties of their hosts. However, we note that our sample size is small, and a larger sample of radio-detected sources is required to study the effects of AGN jets on SF.

This study indicates that NLS1 are low-mass black hole counterparts to BLS1 galaxies with high Eddington ratios. However, their SF properties are similar to each other and also to the SF of MS galaxies, but with large scatter. Although $\text{SFR}-L_{\text{AGN}}$ shows a flat relation for both NLS1 and BLS1 galaxies, when we compared the ratio of SF luminosity with the AGN luminosity, we found that at high stellar masses, AGN feedback could play a role in suppressing SF, but there may be other physical processes as well. Spatially resolved spectroscopic observations in the future hold the key to understanding the complex interplay between AGN activity and their hosts.

Acknowledgements. The funding provided by the Alexander von Humboldt Foundation, Germany is thankfully acknowledged. K.S.K. acknowledges the ESO studentship provided by the European Southern Observatory, Garching.

References

- Abdo, A. A., Ackermann, M., Ajello, M., et al. 2009, *ApJ*, 707, L142
Antón, S., Browne, I. W. A., & Marchã, M. J. 2008, *A&A*, 490, 583
Babić, A., Miller, L., Jarvis, M. J., et al. 2007, *A&A*, 474, 755
Baes, M., Verstappen, J., De Looze, L., et al. 2011, *ApJS*, 196, 22
Baldi, R. D., Capetti, A., Robinson, A., Laor, A., & Behar, E. 2016, *MNRAS*, 458, L69
Baldry, I. K., Driver, S. P., Loveday, J., et al. 2012, *MNRAS*, 421, 621
Becker, R. H., White, R. L., & Helfand, D. J. 1995, *ApJ*, 450, 559
Bentz, M. C., Denney, K. D., Grier, C. J., et al. 2013, *ApJ*, 767, 149
Bollati, F., Lupi, A., Dotti, M., & Haardt, F. 2023, *arXiv e-prints*, arXiv:2311.07576
Boller, T., Brandt, W. N., & Fink, H. 1996, *A&A*, 305, 53
Bongiorno, A., Merloni, A., Brusa, M., et al. 2012, *MNRAS*, 427, 3103

- Boquien, M., Burgarella, D., Roehly, Y., et al. 2019, *A&A*, 622, A103
- Bower, R. G., Benson, A. J., & Crain, R. A. 2012, *MNRAS*, 422, 2816
- Bruzual, G. & Charlot, S. 2003, *MNRAS*, 344, 1000
- Byrne, L., Faucher-Giguère, C.-A., Wellons, S., et al. 2023, arXiv e-prints, arXiv:2310.16086
- Calderone, G., Ghisellini, G., Colpi, M., & Dotti, M. 2013, *MNRAS*, 431, 210
- Cano-Díaz, M., Maiolino, R., Marconi, A., et al. 2012, *A&A*, 537, L8
- Capelo, P. R., Feruglio, C., Hickox, R. C., & Tombesi, F. 2023, in *Handbook of X-ray and Gamma-ray Astrophysics*. Edited by Cosimo Bambi and Andrea Santangelo, 126
- Chabrier, G. 2003, *PASP*, 115, 763
- Charlot, S. & Fall, S. M. 2000, *ApJ*, 539, 718
- Ciesla, L., Charmandaris, V., Georgakakis, A., et al. 2015, *A&A*, 576, A10
- Ciesla, L., Elbaz, D., & Fensch, J. 2017, *A&A*, 608, A41
- Crain, R. A., Schaye, J., Bower, R. G., et al. 2015, *MNRAS*, 450, 1937
- Daddi, E., Dickinson, M., Morrison, G., et al. 2007, *ApJ*, 670, 156
- Dale, D. A., Helou, G., Magdis, G. E., et al. 2014, *ApJ*, 784, 83
- Dickinson, M., Papovich, C., Ferguson, H. C., & Budavári, T. 2003, *ApJ*, 587, 25
- Dimauro, P., Daddi, E., Shankar, F., et al. 2022, *MNRAS*, 513, 256
- Doi, A., Nagira, H., Kawakatu, N., et al. 2012, *ApJ*, 760, 41
- Doi, A., Nakahara, S., Nakamura, M., et al. 2019, *MNRAS*, 487, 640
- Duggal, C., O'Dea, C. P., Baum, S. A., et al. 2024, *ApJ*, 965, 17
- Elbaz, D., Daddi, E., Le Borgne, D., et al. 2007, *A&A*, 468, 33
- Ferrarese, L. & Merritt, D. 2000, *ApJ*, 539, L9
- Fiore, F., Feruglio, C., Shankar, F., et al. 2017, *A&A*, 601, A143
- Gebhardt, K., Bender, R., Bower, G., et al. 2000, *ApJ*, 539, L13
- Grupe, D. & Mathur, S. 2004, *ApJ*, 606, L41
- Gültekin, K., Richstone, D. O., Gebhardt, K., et al. 2009, *ApJ*, 698, 198
- Harrison, C. M., Alexander, D. M., Mullaney, J. R., et al. 2012, *ApJ*, 760, L15
- Hatziminaoglou, E., Fritz, J., & Jarrett, T. H. 2009, *MNRAS*, 399, 1206
- Hickox, R. C., Mullaney, J. R., Alexander, D. M., et al. 2014, *ApJ*, 782, 9
- Hopkins, P. F., Richards, G. T., & Hernquist, L. 2007, *ApJ*, 654, 731
- Hopkins, P. F., Younger, J. D., Hayward, C. C., Narayanan, D., & Hernquist, L. 2010, *MNRAS*, 402, 1693
- Hunt, L. K. & Malkan, M. A. 1999, *ApJ*, 516, 660
- Ichikawa, K., Ricci, C., Ueda, Y., et al. 2017, *ApJ*, 835, 74
- Järvälä, E., Lähteenmäki, A., & Berton, M. 2018, *A&A*, 619, A69
- Järvälä, E., Lähteenmäki, A., Lietzen, H., et al. 2017, *A&A*, 606, A9
- Jarvis, M. E., Harrison, C. M., Thomson, A. P., et al. 2019, *MNRAS*, 485, 2710
- Jha, V. K., Chand, H., Ojha, V., Omar, A., & Rastogi, S. 2022, *MNRAS*, 510, 4379
- Kennicutt, Robert C., J. 1998, *ApJ*, 498, 541
- Kim, C., Woo, J.-H., Jadhav, Y., et al. 2022, *ApJ*, 928, 73
- Klimek, E. S., Gaskell, C. M., & Hedrick, C. H. 2004, *ApJ*, 609, 69
- Kormendy, J. & Richstone, D. 1995, *ARA&A*, 33, 581
- Kotilainen, J. K., León-Tavares, J., Olguín-Iglesias, A., et al. 2016, *ApJ*, 832, 157
- Koutoulidis, L., Mountrichas, G., Georgantopoulos, I., Pouliaxis, E., & Plionis, M. 2022, *A&A*, 658, A35
- Kshama, S. K., Paliya, V. S., & Stalin, C. S. 2017, *MNRAS*, 466, 2679
- Lammers, C., Iyer, K. G., Ibarra-Medel, H., et al. 2023, *ApJ*, 953, 26
- Lang, P., Wuyts, S., Somerville, R. S., et al. 2014, *ApJ*, 788, 11
- Lanzuisi, G., Delvecchio, I., Berta, S., et al. 2017, *A&A*, 602, A123
- León Tavares, J., Kotilainen, J., Chavushyan, V., et al. 2014, *ApJ*, 795, 58
- Madau, P. & Dickinson, M. 2014, *ARA&A*, 52, 415
- Magnelli, B., Lutz, D., Saintonge, A., et al. 2014, *A&A*, 561, A86
- Magorrian, J., Tremaine, S., Richstone, D., et al. 1998, *AJ*, 115, 2285
- Marconi, A., Axon, D. J., Maiolino, R., et al. 2008, *ApJ*, 678, 693
- Marconi, A. & Hunt, L. K. 2003, *ApJ*, 589, L21
- Masoura, V. A., Mountrichas, G., Georgantopoulos, I., & Plionis, M. 2021, *A&A*, 646, A167
- Masoura, V. A., Mountrichas, G., Georgantopoulos, I., et al. 2018, *A&A*, 618, A31
- Mathur, S. 2000, *MNRAS*, 314, L17
- Mathur, S., Fields, D., Peterson, B. M., & Grupe, D. 2012, *ApJ*, 754, 146
- McLeod, K. K. & Rieke, G. H. 1995, *ApJ*, 441, 96
- McLure, R. J. & Dunlop, J. S. 2002, *MNRAS*, 331, 795
- Merritt, D. & Ferrarese, L. 2001, *ApJ*, 547, 140
- Morrissey, P., Conrow, T., Barlow, T. A., et al. 2007, *ApJS*, 173, 682
- Mountrichas, G., Buat, V., Georgantopoulos, I., et al. 2021a, *A&A*, 653, A70
- Mountrichas, G., Buat, V., Yang, G., et al. 2021b, *A&A*, 653, A74
- Mountrichas, G., Buat, V., Yang, G., et al. 2022, *A&A*, 663, A130
- Mullaney, J. R., Alexander, D. M., Aird, J., et al. 2015, *MNRAS*, 453, L83
- Mullaney, J. R., Daddi, E., Béthermin, M., et al. 2012, *ApJ*, 753, L30
- Muzzin, A., Marchesini, D., Stefanon, M., et al. 2013, *ApJ*, 777, 18
- Nagao, T., Murayama, T., Shioya, Y., & Taniguchi, Y. 2002, *ApJ*, 575, 721
- Nandi, P., Stalin, C. S., Saikia, D. J., et al. 2023, *ApJ*, 959, 116
- Netzer, H. 2009, *MNRAS*, 399, 1907
- Ojha, V., Krishna, G., & Chand, H. 2019, *MNRAS*, 483, 3036
- Olguín-Iglesias, A., Kotilainen, J., & Chavushyan, V. 2020, *MNRAS*, 492, 1450
- Orban de Xivry, G., Davies, R., Schartmann, M., et al. 2011, *MNRAS*, 417, 2721
- Osterbrock, D. E. & Pogge, R. W. 1985, *ApJ*, 297, 166
- Paliya, V. S., Parker, M. L., Jiang, J., et al. 2019, *ApJ*, 872, 169
- Paliya, V. S., Pérez, E., García-Benito, R., et al. 2020, *ApJ*, 892, 133
- Paliya, V. S., Stalin, C. S., Kumar, B., et al. 2013, *MNRAS*, 428, 2450
- Papovich, C., Labbé, I., Quadri, R., et al. 2015, *ApJ*, 803, 26
- Peng, Y.-j., Lilly, S. J., Kovač, K., et al. 2010, *ApJ*, 721, 193
- Pilbratt, G. L., Riedinger, J. R., Passvogel, T., et al. 2010, *A&A*, 518, L1
- Popesso, P., Concas, A., Morselli, L., et al. 2019, *MNRAS*, 483, 3213
- Rakshit, S., Johnson, A., Stalin, C. S., Gandhi, P., & Hoenig, S. 2019, *MNRAS*, 483, 2362
- Rakshit, S. & Stalin, C. S. 2017, *ApJ*, 842, 96
- Rakshit, S., Stalin, C. S., Chand, H., & Zhang, X.-G. 2017, *ApJS*, 229, 39
- Rakshit, S., Stalin, C. S., Hota, A., & Konar, C. 2018, *ApJ*, 869, 173
- Rani, P., Stalin, C. S., & Rakshit, S. 2017, *MNRAS*, 466, 3309
- Rihtarič, G., Biffi, V., Fabjan, D., & Dolag, K. 2024, *A&A*, 683, A57
- Sani, E., Lutz, D., Risaliti, G., et al. 2010, *MNRAS*, 403, 1246
- Santini, P., Rosario, D. J., Shao, L., et al. 2012, *A&A*, 540, A109
- Scholtz, J., Alexander, D. M., Harrison, C. M., et al. 2018, *MNRAS*, 475, 1288
- Schreiber, C., Pannella, M., Elbaz, D., et al. 2015, *A&A*, 575, A74
- Shimizu, T. T., Mushotzky, R. F., Meléndez, M., Koss, M., & Rosario, D. J. 2015, *MNRAS*, 452, 1841
- Shimizu, T. T., Mushotzky, R. F., Meléndez, M., et al. 2017, *MNRAS*, 466, 3161
- Silverman, J. D., Lamareille, F., Maier, C., et al. 2009, *ApJ*, 696, 396
- Singh, A., Park, C., Choi, E., et al. 2023, *ApJ*, 953, 64
- Skrutskie, M. F., Cutri, R. M., Stiening, R., et al. 2006, *AJ*, 131, 1163
- Stalewski, M., Ricci, C., Ueda, Y., et al. 2016, *MNRAS*, 458, 2288
- Stanley, F., Alexander, D. M., Harrison, C. M., et al. 2017, *MNRAS*, 472, 2221
- Stanley, F., Harrison, C. M., Alexander, D. M., et al. 2018, *MNRAS*, 478, 3721
- Stanley, F., Harrison, C. M., Alexander, D. M., et al. 2015, *MNRAS*, 453, 591
- Tomczak, A. R., Quadri, R. F., Tran, K.-V. H., et al. 2014, *ApJ*, 783, 85
- Turner, C. S., Miller, H. R., Maune, J. D., & Eggen, J. R. 2022, *MNRAS*, 517, 3257
- Varglund, I., Järvälä, E., Ciroi, S., et al. 2023, *A&A*, 679, A32
- Varglund, I., Järvälä, E., Lähteenmäki, A., et al. 2022, *A&A*, 668, A91
- Vietri, A., Järvälä, E., Berton, M., et al. 2022a, *A&A*, 662, A20
- Vietri, G., Garilli, B., Polletta, M., et al. 2022b, *A&A*, 659, A129
- Viswanath, G., Stalin, C. S., Rakshit, S., et al. 2019, *ApJ*, 881, L24
- Whitaker, K. E., Franx, M., Leja, J., et al. 2014, *ApJ*, 795, 104
- Williams, J. K., Gliozzi, M., & Rudzinsky, R. V. 2018, *MNRAS*, 480, 96
- Wright, E. L., Eisenhardt, P. R. M., Mainzer, A. K., et al. 2010, *AJ*, 140, 1868
- Zhou, H., Wang, T., Yuan, W., et al. 2007, *ApJ*, 658, L13
- Zhuang, M.-Y. & Ho, L. C. 2020, *ApJ*, 896, 108
- Zhuang, M.-Y. & Ho, L. C. 2022, *ApJ*, 934, 130

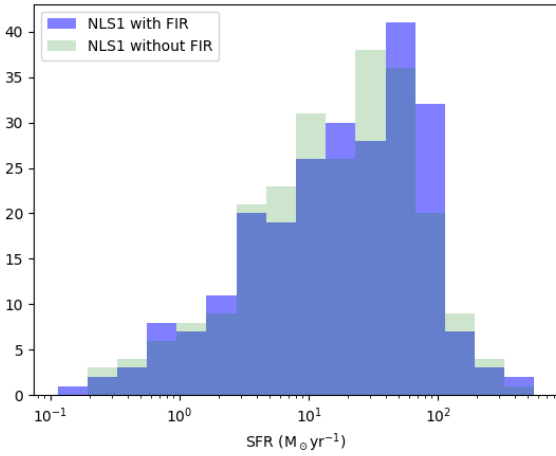
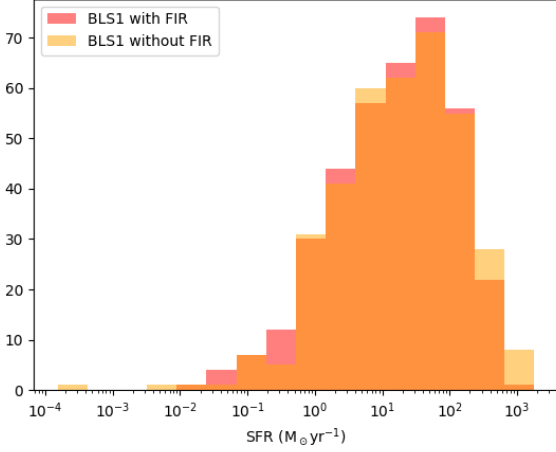


Fig. A.1: Distribution of the SFR with and without the FIR for BLS1 galaxies (top panel) and NLS1 galaxies (bottom panel).

Appendix A: Effect of not including FIR data in the spectral energy distribution modelling

Our current sample of BLS1 and NLS1 galaxies was made with the need for a FIR detection for robust SFR estimates. It has been pointed out by Ciesla et al. (2015) that not including or a lack of FIR data points in the broad-band SED analysis cannot provide a reliable estimate of the SFR. To test this, we performed two sets of SED analyses, one set with FIR points, and the other set without the FIR points. We investigated the obtained physical parameters with and without the FIR photometric points in the SED modelling. We found that when the FIR points are not included, the derived physical parameters are not affected. We show in Fig. A.1 the distribution of the SFR with and without the FIR for the sample of the BLS1 and NLS1 galaxies. The distribution is indistinguishable. We conclude that the non-inclusion of the FIR does not affect the parameters derived in this work.

Appendix B: Effect of redshift on L_{SF}/L_{AGN} versus stellar mass

In Fig. B.1 we show the variation of L_{SF}/L_{AGN} for the low-redshift ($0 < z < 0.3$) and high-redshift ($0.3 \leq z < 0.8$) ranges. For both redshift bins, a decreasing value of L_{SF}/L_{AGN} with in-

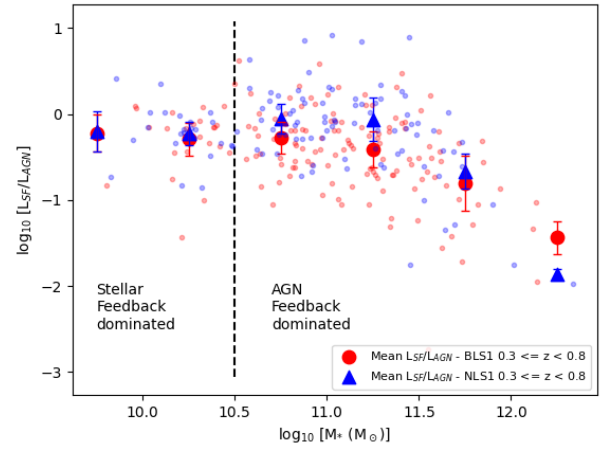
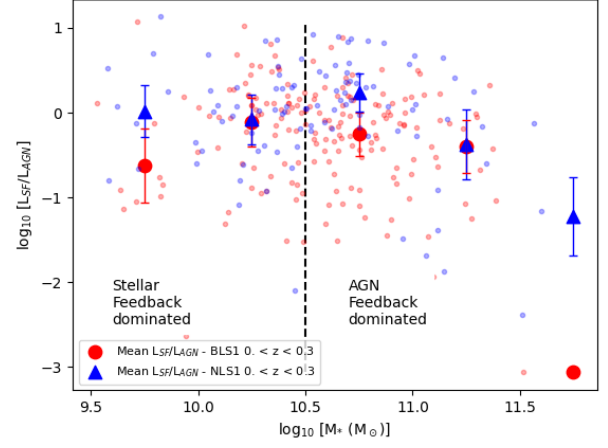


Fig. B.1: Ratio of L_{SF} to L_{AGN} vs. stellar mass for BLS1 galaxies and NLS1 galaxies in the low-redshift (top panel) and high-redshift regions (bottom panel).

creasing stellar mass is observed, but with a large scatter in the low-redshift range. At low redshifts, the BLS1s L_{SF}/L_{AGN} and stellar mass have a correlation co-efficient of -0.14 and a p-value of 0.16, and NLS1s have a correlation coefficient of -0.34 and a p-value of $1.2e-3$. The BLS1 low-redshift sample shows no correlation between L_{SF}/L_{AGN} and M_* . However, the BLS1 low-redshift sample is statistically poor in the highest M_* bin. For the high-redshift range, the correlation coefficient and p-value for the BLS1 L_{SF}/L_{AGN} and stellar mass are -0.37 and $2.7e-5$, respectively, and the correlation coefficient and p-value for the NLS1s at high redshifts is -0.37 and $6.4e-4$, respectively. These values suggest a weak negative correlation between L_{SF}/L_{AGN} and M_* for the high stellar mass range, similar to the values for the full redshift range (Section 4.5 and right panel of Fig. 10). The NLS1 sample at high and low redshifts shows similar correlation coefficients. We therefore conclude that the effect of the redshift on the ratio of L_{SF} to L_{AGN} is negligible for the NLS1 sample.

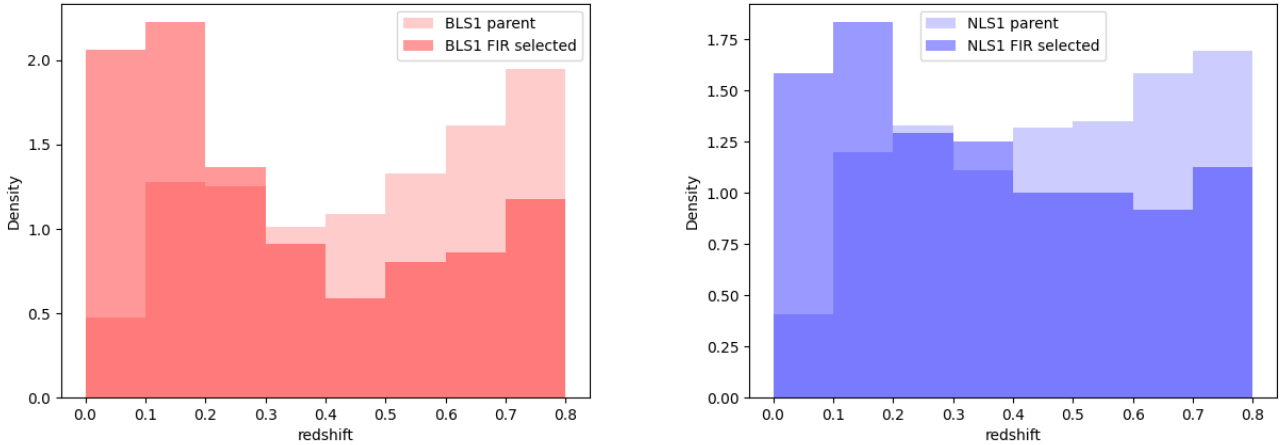


Fig. C.1: Distribution of z for the parent sample and FIR-selected sample for BLS1 galaxies (left panel) and NLS1 galaxies (right panel).

Appendix C: Comparing the parent sample and the Herschel FIR-selected sample

The SDSS-selected parent sample consists of 11101 and 14886 NLS1 and BLS1 galaxies. With the Herschel FIR constraint described in Section 2, our sample for this study consisted of 240 NLS1 galaxies and 373 BLS1 galaxies. Fig.C.1 shows that the FIR-selected sample does not have a similar distribution to the parent sample for the NLS1 and BLS1. The FIR selection biases the sample at high redshifts towards high SFR systems. However, this bias affects both NLS1 and BLS1 equally and does not affect the results of the comparative analysis.

Appendix D: Fluxes

The observed fluxes and their corresponding errors for our sample of BLS1 galaxies and NLS1 galaxies are given in the Tables D.1 and D.2⁴, respectively. We note that the selected sample of 240 NLS1 and 373 BLS1 galaxies was made for the broad-band SED modelling, but the final sample selected for the comparative study was based on the SED fitting (see Section 3). All the fluxes are in units of mJy. The columns are ordered in the following manner: Column 1 - index, Column - SDSS-ID, Column 3 & 4 - RA & Dec, Column 5 - redshift z , Column 6 & 7 - FUV flux & FUV_{err} , Column 8 & 9 - NUV flux & NUV_{err} , Column 10 & 11 - SDSS u' & u'_{err} , Column 12 & 13 - SDSS g' & g'_{err} , Column 14 & 15 - SDSS r' & r'_{err} , Column 16 & 17 - SDSS i' & i'_{err} , Column 18 & 19 - SDSS z' & z'_{err} , Column 20 & 21 - 2Mass J & J_{err} , Column 22 & 23 - 2Mass H & H_{err} , Column 24 & 25 - 2Mass Ks & Ks_{err} , Column 26 & 27 - WISE W1 & $W1_{err}$, Column 28 & 29 - WISE W2 & $W2_{err}$, Column 30 & 31 - WISE W3 & $W3_{err}$, Column 32 & 33 - WISE W4 & $W4_{err}$, Column 34 & 35 - Herschel PACS (green) & $PACS_{err}$ (green), Column 36 & 37 - Herschel PACS (red) & $PACS_{err}$ (red), Column 38 & 39 - Herschel SPIRE PSW & PSW_{err} , Column 40 & 41 - Herschel SPIRE PMW & PMW_{err} , Column 42 & 43 - Herschel SPIRE PLW & PLW_{err} .

⁴ Tables D.1 and D.2 are only available in electronic form at the CDS via anonymous ftp to cdsarc.u-strasbg.fr (130.79.128.5) or via <http://cdsweb.u-strasbg.fr/cgi-bin/qcat?J/A+A/>.